A pseudo-front tracking technique for the modelling of solidification microstructures in multi-component alloys

A. Jacot [a,b,*], M. Rappaz [a]

[a] *Laboratoire de Métallurgie Physique, MX-G, Ecole Polytechnique Fédérale de Lausanne, 1015 Lausanne, Switzerland*
[b] *Calcom SA, Parc Scientifique, Ecole Polytechnique Fédérale de Lausanne, CH-1015 Lausanne, Switzerland*

Abstract

A two-dimensional model for the simulation of microstructure formation during solidification in multi-component systems has been developed. The model is based on a new pseudo-front tracking technique for the calculation of the evolution of interfaces that are governed by solute diffusion and the Gibbs–Thomson effect. The diffusion equations are solved in the primary solid phase and in the liquid using an explicit finite volume method formulated for a regular hexagonal grid. Volume elements located in the liquid phase undergo a transition to interfacial (or mushy) cells before being incorporated in the solid phase. This layer of interfacial elements, which always separates the solid from the liquid sub-domains, permits to handle the displacement of the interface in agreement with the flux condition at the interface. The interface curvature is obtained from the field of the signed distance to the interface, as reconstructed with a PLIC (piecewise linear interface calculation) technique. The concentrations at the solid–liquid interface are calculated using thermodynamic data provided by the phase diagram software THERMO-CALC [Sundman *et al.* CAL-PHAD 1987;9:153]. Different coupling strategies between the microstructure model and THERMO-CALC have been developed, in particular a computationally-efficient direct coupling using the TQ-interface of THERMO-CALC.

After testing the accuracy of the model with respect to curvature calculation, comparisons are made with predictions obtained with the marginal stability theory, a one-dimensional front-tracking method and two-dimensional phase-field simulations of dendritic growth in binary alloys. The model is then used to describe the formation of several grains in an Al–1%Mg–1%Si alloy, as a function of the heat extraction rate and inoculation conditions. It is shown that the model is capable of reproducing the transition between globular and dendritic morphologies. © 2002 Acta Materialia Inc. Published by Elsevier Science Ltd. All rights reserved.

Keywords: Modelling; Phase transformations; Microstructure; Diffusion; Phase diagrams

1. Introduction

The prediction of microstructure formation is a key issue in material science and technology. In casting processes, macrosegregation phenomena occurring on the scale of the ingot are closely connected to the solute redistribution at the dimension of the grains and to the permeability of the mushy zone, both being strongly influenced by the morphology of the primary phase. In aluminium alloys, control of the amount, distribution and size of

---

* Corresponding author. Fax: +41-21-693-5890..
E-mail address: alain.jacot@epfl.ch (A. Jacot).

intermetallic particles during casting and homogenization is of primary importance for the subsequent rolling and forming operations. An important step in the formation of as-cast microstructures is the growth of the primary phase from the melt. This step determines the grain morphology, which can be either globular, globulodendritic or fully dendritic, depending on the inoculation and cooling conditions. Furthermore, the solute redistribution in the solid and liquid phases during primary solidification and the associated solidification path control the type and amount of intermetallic particles that form. A description of the primary phase formation accounting for grain morphology and microsegregation is therefore essential to predict correctly intermetallic particles in as-cast microstructures.

Modelling the evolution of the grain morphology is a very difficult numerical problem for solid–liquid interfaces moving in two- or three-dimensions. Assuming that the phase transformation is mainly governed by diffusion and curvature (Gibbs–Thomson effect), the normal velocity of the interface can be determined from a local solute balance and a calculation of the curvature. However, in practical situations, the undercooling associated with diffusion (typically a few degrees) is usually two orders of magnitude higher than that associated with curvature for primary phase solidification[1]. Worse, the growth direction, shape and kinetics of dendrites are strongly influenced by the *anisotropy* of the chemical potential, which is linked to the anisotropy of the interfacial energy (and its second derivative). In most common metals, the anisotropy of the interfacial energy is very small (a few percents), thus making the problem even more difficult.

A numerical solution to this difficult moving boundary problem can be obtained by using a front-tracking technique based either on boundary element (BEM) [2] or finite element (FEM) methods [3,4]. BEM has been applied successfully to the stationary growth of a free dendrite tip in a thermal gradient [2] but involves heavy mathematical developments, especially for non-stationary

situations. FEM on the other hand involves remeshing procedures and is limited to phase transformations that do not involve important morphology changes. It has been used for example for the calculation of dissolution of pearlite during re-austenitization of steel [4]. In addition to involving large computational times, these techniques do not seem well adapted to the later stages of solidification, when topological changes associated with bridging occur. On the other hand, since the 1990s, the phase field model (PF) has been the subject of numerous research in the field of microstructure predictions [5–16]. The PF method has been applied successfully to the solidification of pure metals [5,6], binary alloys [7–9], eutectic growth [10], three-dimensional growth [6,11] and recently, formulations for multi-component and multiphase systems have been proposed [12,13]. Detailed comparisons have demonstrated that the predicted growth kinetics of a dendrite tip for a binary alloy is in good agreement with experimental results [14] and solvability theory [15], provided that the interface thickness is sufficiently small. However, available computational resources generally impose a lower limit for the interface thickness, which results in artificial non-equilibrium effects. This condition limits presently the application of the PF method to relatively large undercooling and small grain size, unless adaptive mesh refinement techniques are used [9] and/or corrections terms for non-equilibrium effects are added [16].

Pseudo-front tracking methods (PFT) [17–19], which are somewhat in between the PF and front-tracking methods, allow calculations of the primary phase formation to be performed at lower undercooling without the non-equilibrium effects present in PF modelling. However, these techniques usually involve fairly large grid anisotropy, i.e. the growth direction and kinetics of the dendrites tend to be influenced by the orientation and size of the mesh. Such numerical effects are often not very well characterised in simulations of dendritic solidification based upon such methods. One of the objectives of the work presented here is to formulate a PFT model where these effects are minimised and characterised.

The model presented here has for objective the description of the primary phase formation during

---

[1] Unlike eutectics where both undercoolings are comparable.

solidification in multi-component alloys. The model is based on the two-dimensional PFT method which was originally developed for the description of austenitization in Fe–C steels upon heating [17]. The diffusion equations are solved in the liquid and solid phases using an explicit finite volume scheme and special interfacial elements are introduced to account for the boundary conditions on the interface. The original model [17] has been adapted to solidification problems by introducing the Gibbs-Thomson effect and by extending it to multi-component systems. In addition, the model has been coupled with the phase diagram software THERMO-CALC, using different coupling strategies, and in particular a computationally-efficient direct coupling based on THERMO-CALC TQ interface. The accuracy of the numerical method used to calculate diffusion, curvature and cell transition is first assessed through comparisons with sharp interface and PF simulations. The model is then applied to the solidification of an Al–Mg–Si alloy under different cooling and nucleation conditions.

2. Description of the model

2.1. Main assumptions and general structure of the model

Assuming that the temperature is uniform on the scale of the microstructure and that the phase transformation is only governed by the diffusion of the solute element(s) and curvature, growth of the primary phase (α) from the liquid (l) can be described with the following set of equations:

$$\frac{\partial w_i^\nu}{\partial t} = \mathrm{div}[D_i^\nu \mathbf{grad}\, w_i^\nu] \text{ with } i \tag{1}$$

$$= 1,2,...,n \text{ and } \nu = \alpha,\mathrm{l}$$

where n is the number of alloying elements in the multi-component system, w_i^ν is the concentration and D_i^ν the diffusion coefficient of element (i) in phase (ν). Cross diffusion is neglected. The following solute balance must be satisfied at the α/l interface:

$$D_i^\alpha\left[\frac{\partial w_i^{\alpha*}}{\partial n}\right] - D_i^\mathrm{l}\left[\frac{\partial w_i^{\mathrm{l}*}}{\partial n}\right] = \mathbf{v} \cdot \mathbf{n}\, (w_i^{\mathrm{l}*} - w_i^{\alpha*}), \tag{2}$$

where $\mathbf{v}$ is the interface velocity and $\mathbf{n}$ is the normal vector to the interface pointing towards the liquid. The superscript '$*$' denotes concentrations (or gradients) taken at the curved interface. The concentrations $w_i^{\mathrm{l}*}$ and $w_i^{\alpha*}$ in each phase can be deduced from the phase diagram and the interface curvature (see next section).

The diffusion problem made of Eqs. (1) and (2) is solved with an explicit finite volume method formulated for a regular hexagonal fixed grid (see Fig. 1) [17]. A volume element or cell of the mesh has three possible states: solid (α), liquid (l), or interface (mushy). A layer of interface cells always separates liquid cells from α-cells. The solute concentrations in each cell are represented by a set of variables $\{w_i; i=1, n\}$. Additional variables are attributed to interfacial cells: the volumetric solid fraction, g_α, and the interfacial concentrations of the solute elements in the solid and liquid phases, $w_i^{\mathrm{l}*}$ and $w_i^{\alpha*}$. The concentrations, w_i, in these cells correspond to volume averages of the concentrations in the liquid and solid phases, i.e. $w_i = g_\alpha w_i^{\alpha*} + (1-g_\alpha)w_i^{\mathrm{l}*}$.

The first operation performed during one time step is a heat balance based on the assumption of uniform temperature on the scale of the calculation domain:

$$\dot{H} = c_\mathrm{p}\frac{\mathrm{d}T}{\mathrm{d}t} - L\frac{\mathrm{d}g_\alpha}{\mathrm{d}t}, \tag{3}$$

where $\dot{H}$ is the heat extraction rate, c_p the volumetric specific heat and L the volumetric latent heat of fusion. The evolution of the heat extraction rate, $\dot{H}(t)$, being an input of the calculation, Eq. (3) allows the temperature, T, to be calculated once the solidification rate, $\dot{g}_\alpha$, is known from the previous time step (i.e. summation of the variations, δg_α^K, of all the interfacial cells).

The next operation is the calculation of solute diffusion in the liquid and solid phases for each solute element. This is done using an explicit scheme [17]. For interfacial cells, the variations of the average concentrations, δw_i, obtained in this way are transformed into variations of the volume fraction of solid. This is detailed in Section 2.2 together with the state transition algorithm used to displace the interface in the domain. The next operations performed within each time step are con-
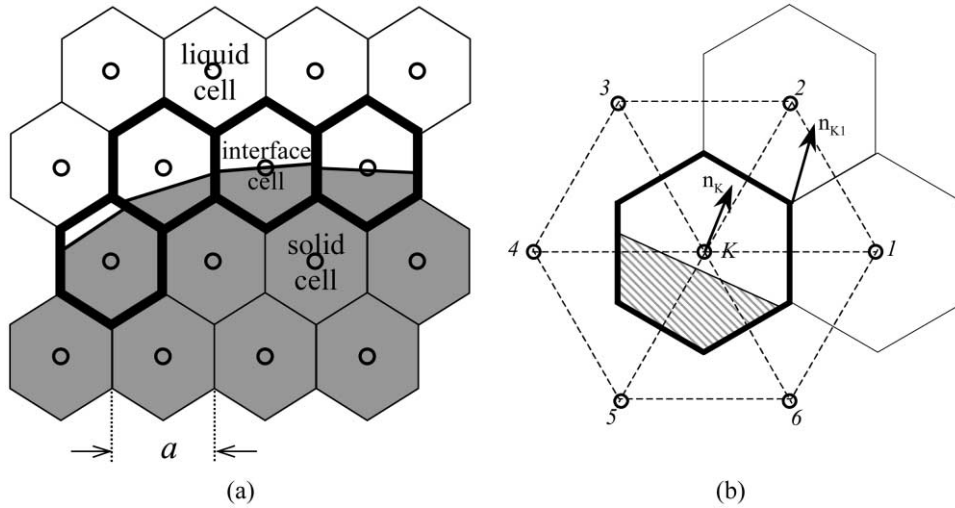
Fig. 1.   Hexagonal grid used to solve the diffusion equation in a two-dimensional domain. Part (a) illustrates the layer of interfacial cells (thick lines) which separates the liquid and solid domains. Part (b) shows one hexagonal cell, its neighbours and the reciprocal lattice.

cerned with the estimation of the interface curvature and the acquisition of thermodynamic data. These procedures are detailed in Sections 2.3 and 2.4, respectively.

2.2. Solute diffusion and interface displacement

The diffusion of the solute elements in the solid and liquid phases is described using an explicit finite volume method formulated for the hexagonal grid shown in Fig. 1. A solute balance is performed in each cell K and for each solute element i [17]:

$$V\frac{\delta w_i^K}{\delta t} = \sum_{I=1}^{6} SJ_i^{I,K} \tag{4}$$

with

$$V = \frac{\sqrt{3}}{2}a^2 \text{ and } S = \frac{a}{\sqrt{3}} \tag{5}$$

where a is the cell size as defined in Fig. 1, V and S are the surface and edge length of the cells, respectively, δt is the time step, δw_i^K is the variation of solute i in cell K and $J_i^{I,K}$ is the flux of solute i between cells I and K. This solute flux is calculated differently according to the state of the two cells.

If cells I and K belong to the same phase v:

$$J_i^{I,K} = D_i^v \frac{w_i^I - w_i^K}{a} \quad v = \alpha \text{ or } l. \tag{6}$$

If cell I is of interfacial type and the neighbour cell K belongs to phase v(i.e. the face in between is totally made of phase v on first approximation):

$$J_i^{I,K} = D_i^v \frac{w_i^{v,I*} - w_i^K}{\left(\frac{1}{2} + g_v^I\right)a} \quad v = \alpha \text{ or } l \tag{7}$$

where $w_i^{v,I*}$ is the concentration of solute i at the interface in phase v in cell I and g_v^I is the fraction of phase v in cell I. The factor multiplying a at the denominator accounts for the position of the interface in the interfacial cell[2].

If both I and K are interfacial cells:

$$J_i^{I,K} = D_i^\alpha \varphi^\alpha \frac{w_i^{\alpha,I*} - w_i^{\alpha,K*}}{a} + $$
$$D_i^l(1-\varphi^\alpha)\frac{w_i^{l,I*} - w_i^{l,K*}}{a} \tag{8}$$

---

[2] If $g_v^I = 1/2$ the interfacial concentration is taken in the middle of cell I; if $g_v^I = 0$, the interface is located on the face between cells I and K and the distance is $a/2$; if $g_v^I = 1$ the interface is on the opposite face and the distance is $3a/2$.

where φ^{α} is an estimation of the fraction of solid along the common edge to cells I and K. A value for φ^{α} is obtained from the interface reconstruction algorithm described in Section 2.3.

In the cells that are entirely solid or liquid, the evolution of the concentrations is directly given by Eq. (4). For interfacial cells, the variations of concentration obtained with (4) represent an average over the liquid and solid phases. These quantities are converted into a variation of solid fraction using the lever rule approximation at the level of each interfacial cell. Assuming 'thermodynamic equilibrium' at the interface (modified by curvature), the actual temperature of the domain is related to the interfacial concentrations according to the following equation (the index of the interfacial cell is omitted for the sake of clarity):

$$T = T_{L}^{\alpha}(w_1^{1*} + \delta w_1^{1*},...,w_n^{1*} + \delta w_n^{1*}) - \Delta T_r \quad (9)$$

where $T_{L}^{\alpha}(w_1,...,w_n)$ is a function giving the liquidus temperature for a given set of concentrations, $(w_i^{1*} + \delta w_i^{1*})$ is the new concentration of solute i at the interface in the liquid and ΔT_r is the curvature undercooling. The calculation of ΔT_r is described in Section 2.3.

Assuming that the concentrations on the scale of the interfacial cells are uniform, a lever rule can be written for each solute element:

$$w_i + \delta w_i = (1 +$$
$$g_{\alpha}[k_i^{1,\alpha}(w_1^{1*} + \delta w_1^{1*},...,w_n^{1*} + \delta w_n^{1*}) - 1]) \quad (10)$$
$$(w_i^{1*} + \delta w_i^{1*})$$

where the $k_i^{1,\alpha}$ are the non-constant partition coefficients and δw_i the average variations of concentration obtained with (4).

Eqs. (9) and (10) form a set of $(n+1)$ equations, the resolution of which provides the new volume fraction of solid of the corresponding cell, g_{α}, and the n variations of the solute concentrations in the liquid, δw_i^{1*}. A Newton–Raphson iterative algorithm is used to solve this non-linear problem. Each iteration consists of solving a linear system composed of the following set of equations:

$$T + \Delta T_r = T_{L}^{\alpha}(w_1^{1*},...,w_n^{1*}) + \sum_i \frac{\partial T_{L}^{\alpha}}{\partial w_i^{1*}} \delta w_i^{1*} \quad (11)$$

$$\delta w_i = w_i^{1*}(k_i^{1,\alpha} - 1)\delta g_{\alpha} +$$

$$(1 + g_{\alpha}(k_i^{1,\alpha} - 1))\delta w_i^{1*} + g_{\alpha}w_i^{1*}\sum_j \frac{\partial k_i^{1,\alpha}}{\partial w_j^{1}} \delta w_j^{1*} \quad (12)$$

with $i = 1,...,n$.

Provided the cell size is small with respect to the diffusion layer, this procedure is equivalent to solve the interface solute balance expressed by Eq. (2). A mathematical development showing this equivalence is presented in the Appendix.

When g_{α} in an interfacial cell becomes larger than unity, the cell is attributed to the α phase. All the liquid cells which are adjacent to this newly solid cell become interfacial cells (with g_{α}=0) so that liquid and solid cells are never in direct contact. Similarly, if g_{α} falls below zero in a cell (local remelting), the cell becomes liquid and the solid neighbours are transformed into interfacial cells (with g_{α}=1).

2.3. Interface curvature

The curvature of the interface is obtained through the calculation of an additional field: the signed distance to the interface, δ. This quantity is negative in the solid, positive in the liquid and null on the interface. The calculation of δ requires a precise knowledge of the position of the interface. The PLIC algorithm (piecewise linear interface calculation), which was originally developed for fluid flow problems [20], is first used to reconstruct the interface from the solid fraction field. The PLIC method is based on the assumption that the interface is a straight line inside any given interfacial cell. The position of the linear segment representing the interface in a cell, K, is univocally defined from the solid fraction in the cell, g_{α}^{K}, and the normal vector to the interface, $\mathbf{n}^{K}$.

The interface curvature is obtained through the following algorithm:

1. *Calculation of the PLIC segments.* Each interfacial cell K is 'filled' with a portion of solid, perpendicularly to $\mathbf{n}^{K}$ (normal vector to the interface obtained at previous time step or iteration) and up to a value of g_{α}^{K} (see [21] for details).
2. *Calculation of* δ. δ is defined as the shortest dis-

tance to the PLIC segments present in the calculation domain. This quantity is calculated at the centres of the hexagonal cells. For a better computation efficiency, the calculation of the distance field is limited to a narrow region around the interface and the minimum of the distance is searched only among the closest PLIC segments.

3. *Calculation of the normal vector to the interface in each interfacial cell* K. First, in each triangle of the reciprocal lattice (dashed lines of Fig. 1b), a normal vector is calculated using the following expression:

$$\mathbf{n}^{\mathbf{KI}} = \frac{(\mathbf{grad}\ \delta)^{KI}}{|(\mathbf{grad}\ \delta)^{KI}|} \tag{13}$$

where *KI* is an index standing for the triangle of the reciprocal mesh. The gradient of δ in triangle *KI* ,$(\mathbf{grad}\ \delta)^{KI}$, is calculated using a linear function for δ, defined by the values obtained in (2) at the corners of the triangle (which are also cell centres). The vector $\mathbf{n}^K$ in each interfacial cell *K* is then obtained by averaging the normal vectors obtained in the six neighbouring triangles:

$$\mathbf{n}^{\mathbf{KI}} = \sum_{I\ =\ 1}^{6} \mathbf{n}^{\mathbf{KI}}. \tag{14}$$

4. *Return to (1) if convergence is not reached*
5. *Calculation of the interface curvature.* The following geometrical relationship is used:

$$\kappa = \text{div }\mathbf{n}. \tag{15}$$

The latter expression is evaluated numerically in each interfacial cell using the vectors $\mathbf{n}^{KI}$ and first order derivatives.

Fig. 2 illustrates the calculated distance field and the reconstructed interface obtained with the PLIC algorithm in a small region in the vicinity of the interface. As can be seen, the PLIC segments of adjacent interfacial cells are not necessarily connected, although they almost match if the mesh size is small with respect to the radius of curvature of the interface.

The curvature undercooling is calculated with the following expression:

$$\Delta T_{\mathrm{r}}^{K} = \frac{\kappa^{K}(\sigma(\theta)\ +\ \sigma''(\theta))}{\Delta s_{\mathrm{f}}} \tag{16}$$

Δs_{f} is the volumetric entropy of melting and $\sigma(\theta)$ is the surface tension, which is a function of the angle θ defining the orientation of the interface ($\sigma''(\theta)$ is the second derivative with respect to θ). The surface tension is assumed to obey the following θ-dependence:

$$\sigma(\theta) = \sigma_0\eta(\theta) = \sigma_0[1\ +\ \varepsilon_m\cos(m(\theta-\theta_0))] \tag{17}$$

where σ_0 is an average value, ε_m is the relative variation (anisotropy), *m* is the symmetry order and θ_0 defines the preferred growth direction of the interface (i.e. the maxima of the interfacial energy or the minima of the chemical potential).

2.4. Thermodynamic data

The thermodynamic data needed for the calculation are the liquidus temperature T_{L}^{α} and the partition coefficients k_i^{α} as a function of the liquid compositions $\{w_i^{\mathrm{l}}\}$. For binary systems, this information could be obtained easily from published phase diagrams. However, this approach would be difficult to follow for ternary and nearly impossible for more complex systems. The use of thermodynamic calculation tools, such as the CALPHAD approach [22], clearly appears to be the appropriate method for multi-component systems. Several strategies to couple CALPHAD calculations with the PFT method have been implemented and compared as follows.

2.4.1. Data tabulation

This approach is an extension of the method used by X. Doré for the Al–Mg–Si system [21]. The liquidus temperatures and the partition coefficients are calculated with THERMO-CALC [1] for a fixed grid of concentrations and stored in a separate file before starting the microstructure calculation. The grid used to tabulate the thermodynamic data has a dimension equal to the number of solute elements. For example, it is a square grid for a ternary system, a cubic grid for a quaternary system and a 'hypercubic grid' for systems of higher orders. During the microstructure calculation, multi-linear functions are used to interpolate the data stored in the tabulation grid.

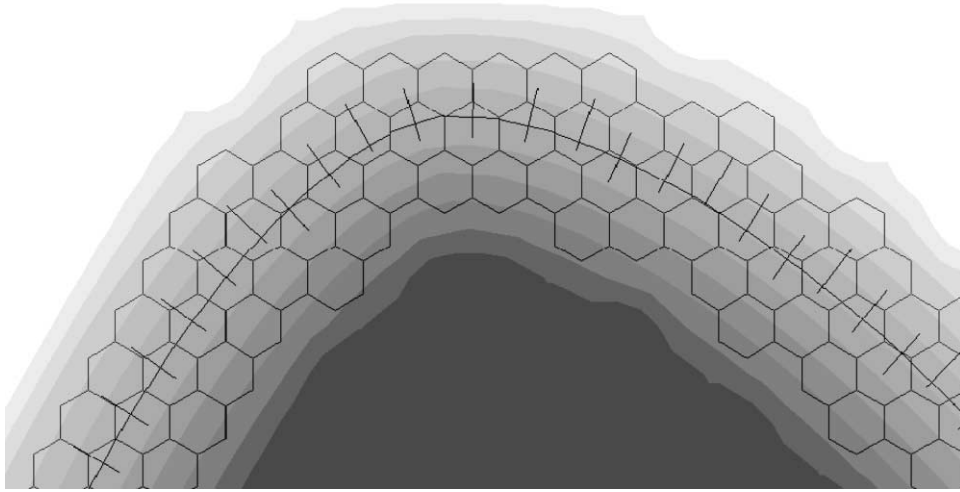The possible stability of a secondary phase β is

Fig. 2.   PLIC segments, normal vectors and distance field (grey levels) used to describe the interface in the PFT model.

tested at each time step by a calculation of the liquidus temperature of β, as a function of the average composition of the liquid at the interface, $(\bar{w}_1^{1*},...,\bar{w}_n^{1*})$. The function $T_L^{\beta}(\bar{w}_1^{1*},...,\bar{w}_n^{1*})$ is estimated with the same tabulation method as $T_L^{\alpha}(\bar{w}_1^{1*},...,\bar{w}_n^{1*})$. The calculation is stopped when $T < T_L^{\beta}$, which means that a eutectic or peritectic phase has been reached.

Although this procedure may be too heavy in complex multi-component systems (due to large tabulation files), it proved to be a reasonable and robust approach for systems up to four alloying elements. Inaccuracies may occur for phase diagrams containing abrupt changes of the liquidus slope or partition coefficients.

2.4.2. Direct coupling with THERMO-CALC

In this approach, the phase diagram software THERMO-CALC is accessed for each interfacial cell and at each time step while the microstructure model is running (so-called direct coupling). In this case the mathematical problem composed of Eqs. (9) and (10) does not need to be solved. The new temperature (corrected for the Gibbs–Thomson effect), $T + \Delta T_r$, and the average composition in the mushy cell are input to THERMO-CALC, which provides in feedback the solid fraction and the composition of the liquid and solid phases at the

new thermodynamic equilibrium. The TQ-library of FORTRAN subroutines of THERMO-CALC was used to implement this coupling. Although general and easy to implement, this approach is very computationally intensive and exposed to robustness problems.

2.4.3. Optimised direct coupling with THERMO-CALC

This approach involves also a direct coupling between THERMO-CALC and the microstructure model via the TQ-interface. However, the number of thermodynamic equilibrium calculations is limited in order to speed up the calculation. The approach is based on the assumptions that the differences between the interfacial concentrations within the calculation domain can be approximated by linear functions. More precisely, the following linear dependencies of T_L^{α} and k_i^{α} are assumed:

$$T_L^{\alpha}(w_1,...,w_n) = T_L^{\alpha}(\bar{w}_1^{1*},...,\bar{w}_n^{1*}) \qquad (18)$$

$$+ \sum_{i=1}^{n} \frac{\partial T_L^{\alpha}}{\partial w_i}(w_i - \bar{w}_i^{1*})$$

$$k_i^{\alpha}(w_1,...,w_n) = k_i^{\alpha}(\bar{w}_1^{1*},...,\bar{w}_n^{1*}) \qquad (19)$$

$$+ \sum_{i=1}^{n} \frac{\partial k_i^{\alpha}}{\partial w_i}(w_i - \bar{w}_i^{1*})$$

where $(\bar{w}_1^{1*}, ..., \bar{w}_n^{1*})$ is the set of mean concentrations in the liquid of all the interfacial cells at the previous time step. At each time step, $(n + 1)$ equilibrium calculations are performed in order to update T_L^α, $\{k_i^\alpha\}$ and their derivatives with respect to each of the n solute elements. Additional calculations are needed to test the stability of the secondary phases.

3. Results and discussion

3.1. Validation tests

The objective of the first test was to estimate the accuracy of the numerical procedure used to calculate the interface curvature. For this test, a sinus shape was imposed to the solid/liquid interface so that the curvature calculated numerically could be compared easily with an analytical solution. The solid fraction in each cell was calculated analytically using the sinus equation of the interface. After initialization, the curvature was estimated with the procedure described in Section 2.3. The evolutive problem was not solved in this case.

Fig. 3 shows a comparison of the curvature obtained analytically and numerically for a wavelength of about $27a$ and an amplitude of $6.25a$. As can be seen, excellent agreement is obtained between the numerical results and the analytical solution under the present conditions. Obviously,
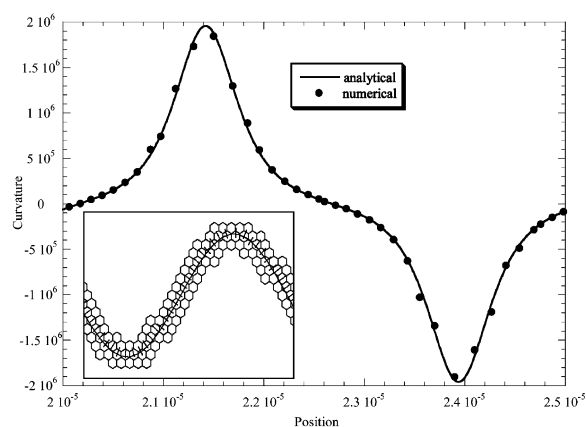

Fig. 3. Curvature of a sinus-shaped interface obtained analytically and numerically using the distance field technique. The insert shows the PLIC segments used to represent the position of the interface in the hexagonal grid.

the accuracy depends on the mesh used to resolve the sinus shape. However, it is satisfactory to obtain such an accuracy, for a mesh which is relatively coarse with respect to the smallest radius of curvature of the interface (see insert in Fig. 3).

The second validation test was aimed at verifying the ability of the model to correctly solve the mathematical problem composed of Eqs. (1) and (2) in a mono-dimensional case. The objective was to compare the diffusion field calculated with the PFT method and a fixed grid, with that obtained with a one-dimensional finite difference program based on a front tracking approach and a Landau transformation [17]. A model alloy with a liquidus slope of $-500K$, a partition coefficient of 0.5 and a nominal concentration of 0.05 was used for this test. As an initial condition, the system was set at thermodynamic equilibrium 1K under the liquidus temperature, which corresponds to a solid fraction of 7.7%. The solid/liquid interface was set at 0.77 μm from the left border of a 10 μm domain, and the concentrations were initialised according to equilibrium. The calculation was performed using a heat extraction rate of -1.25×10^8 Wm^{-3} (equivalent to cooling rate of $-50K$ s^{-1}). The domain was enmeshed with a grid of 100 cells along the main dimension and two cells in height. The small height permits to avoid interface instabilities, which tend to arise due to constitutional undercooling. Adiabatic boundary conditions were applied on the lateral borders whereas periodic conditions were used on the top and bottom borders. An evolutive grid of 50 nodes in both the liquid and solid phases was used to run the one-dimensional front tracking program [17]. The other parameters of the PFT calculation are given in Table 1 (calculation A).

Fig. 4 shows the concentration profiles obtained with the two models at 10 different times. As can be seen, the agreement is very good. The only difference that can be observed is for the concentration jump at the interface; this is spread over one mesh layer in the two-dimensional PFT model, whereas there is a sharp transition for the one-dimensional front tracking model. Small differences are also observed at the very end of solidification when the size of the liquid region is of the order of the cell dimension.

Table 1
Parameters of the calculations

Calculation	A	B	C	D	E
Alloy					
System	Model alloy	Al–Cu	Ni–Cu	Al–Mg–Si	Al–Mg–Si
Phase diagram	$m_l = -500K$ $k^\alpha = 0.5$	From [25]	From [7]	From [25]	From [25]
Nominal composition	0.05	0.02	0.408	$w_{Mg} = 0.01$ $w_{Si} = 0.01$	$w_{Mg} = 0.01$ $w_{Si} = 0.01$
Thermal conditions					
$\dot{H}$ [Wm^{-3}]	-1.25×10^8	–	–	-3.9×10^7	-2.08×10^8
L [Jm^{-3}]	10^9	–	–	9.5×10^8	9.5×10^8
ρc_p [Jm^{-3}K^{-1}]	2.5×10^6	–	–	2.6×10^6	2.6×10^6
Imposed ΔT [K]	–	1	20.5	–	–
Surface energy					
$\sigma_0 / \Delta s_f$ [Km]	1×10^{-7}	5×10^{-7}	2.5×10^{-7}	2.5×10^{-7}	2.5×10^{-7}
ε_4	0	0.04	0.04	0.04	0.04
Diffusion					
D^α[m^{2}s^{-1}]	10^{-13}	5×10^{-10}	10^{-13}	$D^\alpha_{Mg} = 1.24 \times 10^{-4}e^{-130400/RT}$ [26] $D^\alpha_{Si} = 2.02 \times 10^{-4}e^{-136000/RT}$ [26]	
D^l[m^{2}s^{-1}]	10^{-11}	5×10^{-9}	10^{-9}	$D^l_{Mg} = 0.99 \times 10^{-4}e^{-71587/RT}$ [27] $D^\alpha_{Si} = 0.11 \times 10^{-4}e^{-49022/RT}$ [28]	
Solid seed					
Number	1	1	1	20	4
Size [µm]	0.77	5	0.2	5	5
Position	Left border	Centre	Centre	Random	Random
θ_0	0°	11°	11°	Random	Random
Space and time					
Domain size [µm^2]	10×0.2	400×400	9×9	500×433	500×433
Final time [s]	10	3	1.6×10^{-4}	27.2	5.05
PFT					
Number of cells	100×2	400×464	900×1038	400×400	400×400
CPU time[a]	3.5 min	29 h	36 h	70 h	112 h
PF					
λ [m]		0.5×10^{-6}	1.0×10^{-8}		
μ_k [m^{1}K^{-1}s^{-1}]		1.5×10^{-3}	$6.6 \times 10^{-3}/3.3 \times 10^{-3}$		
Number of cells		400×400	900×900		
CPU time[a]		16 h	8 h		

[a] Processor SGI R10000@250 MHz.

3.2. Comparison with PF simulations for binary alloys

In order to assess the ability of the model to correctly predict the grain morphology in two dimensional problems, systematic comparisons were performed between the PFT method and a PF model for binary alloys. The PF model used for these tests is close to the formulation presented by Tiaden *et al.* [8]. The evolution of the solid/liquid interface is described through the following phase equation:

$$\frac{\dot{\phi}}{\mu_k} = \Gamma \left[\nabla^2 \phi - \frac{\partial}{\partial x}\left(\eta \frac{d\eta}{d\theta}\frac{\partial \phi}{\partial y}\right) + \frac{\partial}{\partial y}\left(\eta \frac{d\eta}{d\theta}\frac{\partial \phi}{\partial x}\right) \right.$$
$$\left. - \frac{\phi(1-\phi)(1-2\phi)}{\lambda^2} \right] +$$
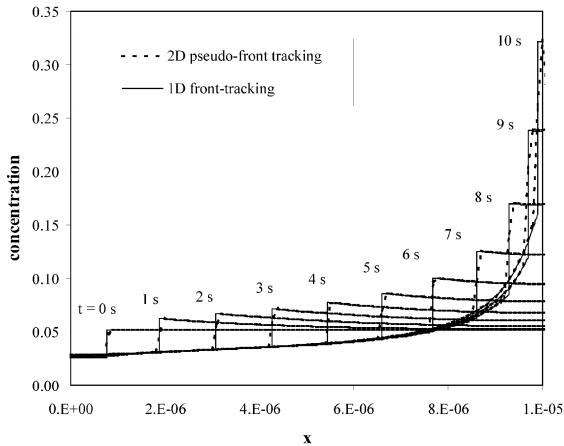$$\frac{5\phi^2(1-\phi)^2}{\lambda}m_l(w^l - w^{l*}) \qquad (20)$$

Fig. 4. Comparison of concentration profiles obtained with the two-dimensional PFT model and a one-dimensional sharp interface model.

where ϕ is the PF which varies smoothly from 0 in the liquid to 1 in the solid, μ_k is the interface kinetic coefficient, $\Gamma = \sigma_0/\Delta S_f$ is the isotropic Gibbs–Thomson coefficient, η is the anisotropy function defined in Eq. (17), λ is the interface thickness, m_l is the liquidus slope and w^{l*} is the equilibrium composition of the liquid given by the phase diagram. The symbol w^l denotes the local composition of the liquid defined as:

$$w^l = \frac{w}{1 - \phi + k^\alpha \phi} \quad . \tag{21}$$

The evolution of the concentration, w, is obtained with the following diffusion equation:

$$\dot{w} = \nabla \cdot \left[\tilde{D} \left(\nabla w + \frac{(1-k)w}{1 - \phi + k^\alpha \phi} \nabla \phi \right) \right] \tag{22}$$

with

$$\tilde{D} = D^\alpha + \frac{1 - \phi}{1 - \phi + k^\alpha \phi} (D^l - D^\alpha). \tag{23}$$

Eqs. (20) and (22) were solved using an explicit finite difference method and a regular square grid.

A case of isothermal solidification in an Al–2 wt%Cu alloy at a constant undercooling $\Delta T = 1$ K was selected for this test. A small solid seed with a crystallographic orientation $\theta_0 = 11°$ was placed at the centre of a 400 μm×400 μm domain

as an initial condition. The crystal orientation was voluntarily misaligned with respect to the grid in order to reveal potential grid anisotropy effects. Periodic boundary conditions and a grid spacing of 1 μm were used both in PF and PFT simulations. The other parameters are given in Table 1 (calculation B).

Fig. 5 shows the position of the interface and concentration maps at two different times obtained with the PFT and PF models. Although small difference can be noticed between the concentration fields, the overall agreement is very good. No particular effects of grid anisotropy are observed, neither in PFT nor in PF, since the dendrite arms are correctly oriented at 11° with respect to the horizontal and vertical axes, despite the use of hexagonal or square grids.

The difference between the PF and PFT results can better be observed on Fig. 6, where concentration profiles measured along a dendrite axis (see line illustrated on Fig. 5) have been reported. The continuous lines on Fig. 6 correspond to profiles obtained with a mesh of 400×400 nodes (400×464 cells for PFT), whereas dashed lines are results using coarser meshes (200×200 for PF and 200×232 for PFT). Some discrepancy is observed between the interface position predicted by PF and PFT, but, as expected, it decreases as the mesh is refined. Calculations with even finer meshes would permit to verify whether convergence between PF and PFT is reached eventually. Although this investigation could not be carried out due to excessive computation times, it is expected that small differences would ever remain due to the attachment kinetic term, which is present in the PF model and neglected in PFT. The kinetic undercooling that can be estimated from the dendrite tip velocity is about 0.016 K for the present conditions and parameters ($\mu_k = 1.5 \times 10^{-3}$ ms^{-1}K^{-1}). This undercooling corresponds to a reduction of 1.6% in supersaturation. Although this effect is almost negligible in the present case, it must be pointed out that the real kinetic effect expected under such solidification conditions is one or two order of magnitudes lower. PF simulations performed with an interface thickness higher than the physical value are also known to introduce artificial non-
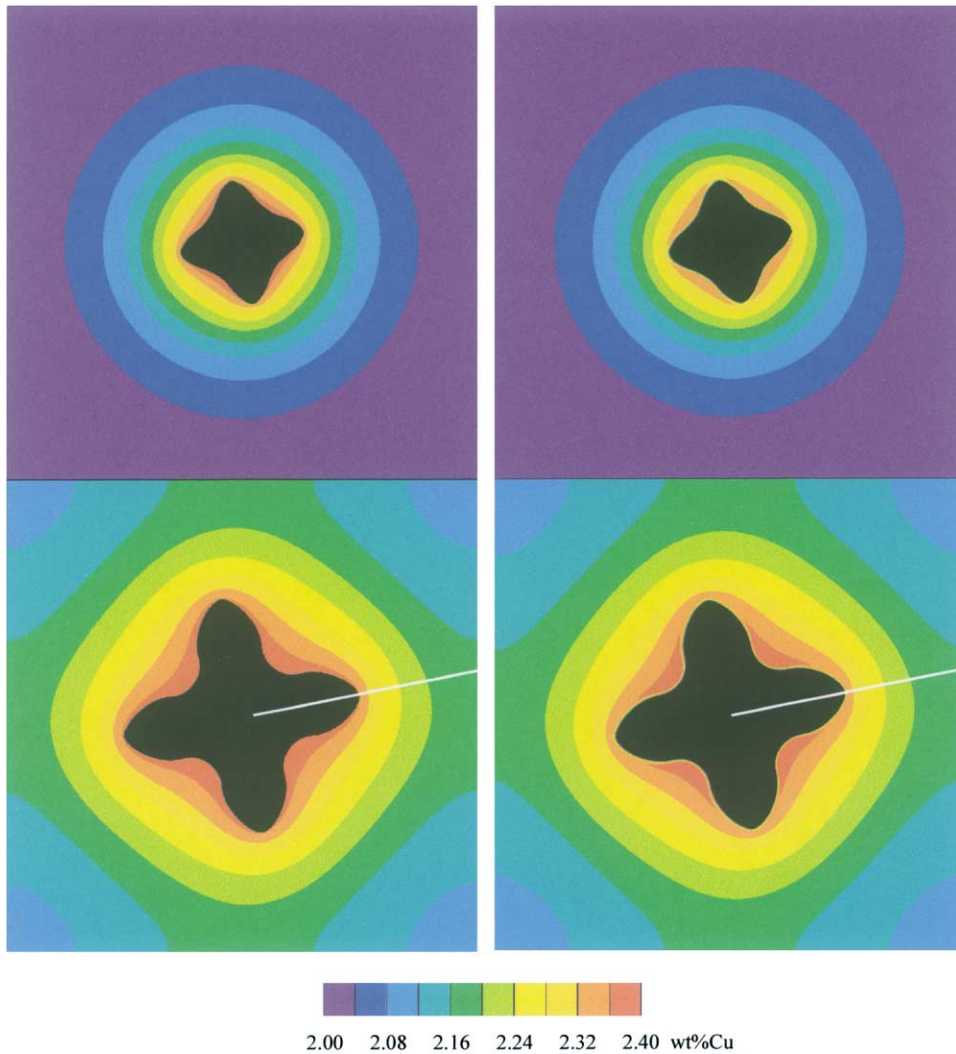
Fig. 5.   Concentration field calculated with the PFT (left) and PF (right) models for an Al–2 wt%Cu dendrite growing at a constant undercooling of 1K. The domain dimensions are 400 μm×400 μm. The time is 1 s for the upper two figures and 3 s for the lower ones.

equilibrium effects [16], whose role is unclear in the present test.

The difference between fine and coarse mesh calculations appears to be higher in PF than in PFT simulations (see Fig. 6). It is believed that convergence of the results with respect to the space discretization would be reached sooner in PFT than in PF under the present conditions. However, further comparisons would be needed to determine the exact convergence behaviour. On the other

hand, the CPU time of PFT calculations is about twice that of PF ones (see Table 1).

In the present calculation, the diffusion layer ahead of the moving solid/liquid interface interacts almost immediately with the diffusion layer coming from the other side of the grain (since periodic boundary conditions are used, it does not interact directly with the boundary of the domain). This situation is far from a free dendritic growth as found under directional solidification or as
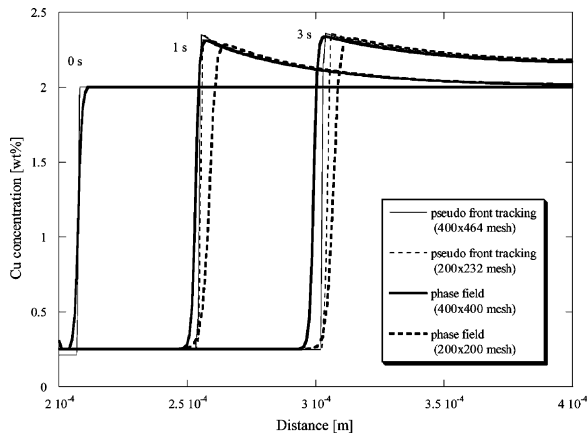
Fig. 6. Concentration profiles along the primary dendrites arms (white line in Fig. 5) obtained with the PTF and PF models, with different mesh resolutions.

described in analytical model of dendritic growth [23]. It is, however, quite representative of typical solidification conditions for grain-refined alloys, where large grain densities and low undercooling are generally the rule.

Nevertheless, it was also interesting to apply the PFT model to a free dendritic growth problem, with the objective to compare the solution with other approaches such as marginal stability theory [23]. The conditions used by Warren and Boettinger in [7] for a free Ni–Cu dendrite growing at a high supersaturation was considered for this test. The PFT results were compared with marginal stability theory and with a PF simulation performed with the original formulation of [7]. A calculation domain of 9 μm×9 μm and periodic boundary conditions were used for this test. As in previous simulations, the crystal orientation θ_0 was set to 11° to avoid any symmetry relationship between the dendrite and the mesh.

Prior to compare PFT and PF results, a sensitivity analysis with respect to the important numerical parameters was performed on both models. The mesh used for PFT simulations was refined until the dependence of the results with respect to the grid resolution was no longer significant. A mesh of 900×1038 hexagonal cells was finally retained for the comparison. PF results proved to be less mesh-dependent, but the growth rate and the tip radius of the dendrite were strongly influ-

enced by the choice of the kinetic coefficient and to some extent by the interface thickness. Since attachment kinetic is neglected in PFT, it was tried to perform PF calculations using a kinetic coefficient as high as possible. Unfortunately, PF calculations at high kinetic coefficient are difficult to perform for numerical reasons. The parameters finally selected for the comparison are $\mu_k=6.6\times10^{-3}$ m^{-1}K^{-1}s^{-1} and $\lambda=10$ nm [see also Table 1(calculation C)].

Fig. 7 shows the results obtained with the PFT and PF models for a time after nucleation of 1.6×10^{-4} s. As can be seen, the PF dendrite grows at lower velocity and with a coarser tip as compared with the PFT dendrite. This difference is certainly due to non-equilibrium effects, which are considered in the PF model only. The kinetic undercooling at the dendrite tip present in PF simulation was estimated to 3–4K (deduced from the tip velocity at steady state). Compared to the 20K solutal undercooling, this term has certainly an important influence on the growth morphology and could explain the differences observed. The PF model also accounts for solute trapping, which tends to increase the growth rate. This effect seems to be smaller than the attachment kinetics, since the predicted growth rate is smaller than in PFT.

The PF and PFT results were also compared to the marginal stability theory [23]. The steady-state growth rates obtained with the three approaches are reported in Table 2 and the contours of the dendrite tips are presented on Fig. 8. As expected, in presence of surface energy anisotropy, both the PFT and PF models predict a sharper tip and a higher growth velocity than the marginal stability theory. Due to attachment kinetics, the PF model predicts a coarser tip radius and a lower growth rate than PFT. A PF calculation performed at lower kinetic coefficient ($\mu_k=3.3\times10^{-3}$ m^{-1}K^{-1}s^{-1}) lead to a growth rate which is even lower than marginal stability (see Table 2). This confirms the importance of non-equilibrium effects in the PF simulation.

It appears from this investigation that the presence of kinetic undercooling and solute trapping in the PF model makes detailed comparison between PF and PFT difficult to perform. Similarly, comparisons between marginal stability theory and
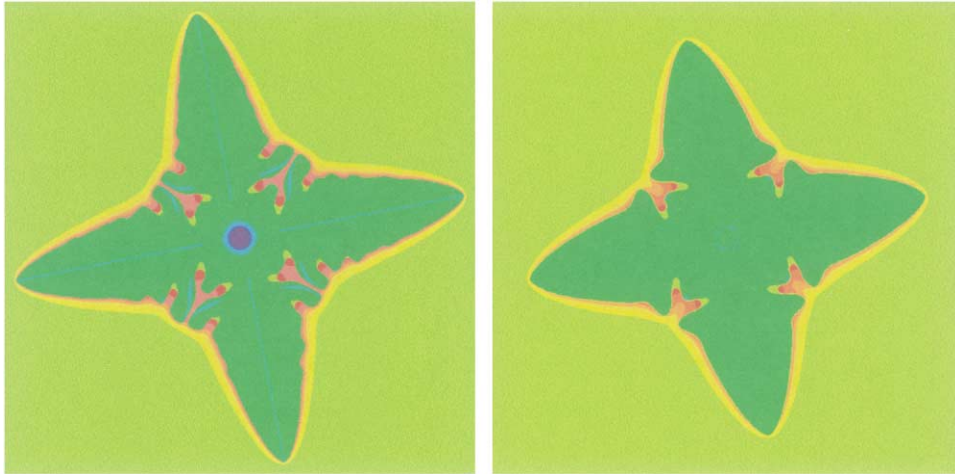
Fig. 7. Ni–Cu dendrite computed with the PFT (left) and PF (right) models. The time is 1.6×10^{-4} s after nucleation. The mesh resolution is 900×1038 for the PFT, and 900×900 for the PF.

Table 2
Steady state growth rate of a free dendrite predicted by different models for a constant 20K undercooling and a Ni–0.408Cu alloy

Marginal stability theory	PF (WB model)	PFT
2.19 cm/s	2.23 cm/s ($\mu_k=6.6\times10^{-3}$ $ms^{-1}K^{-1}$) 1.09 cm/s (3×10^{-3} $ms^{-1}K^{-1}$)	2.91 cm/s

Fig. 8. Shape of the dendrite tip predicted with PFT, PF and marginal stability theory.

numerical simulation is also difficult, given that surface tension anisotropy is not considered in the theoretical model. In spite of these difficulties, this investigation permitted to verify that the growth kinetics and the dendrite shape predicted with the PFT is in reasonable agreement with other approaches. Furthermore, the differences could always be explained qualitatively by considering the assumptions made in each model.

Comparisons with solvability theory [24], which accounts for surface tension anisotropy, would permit to better assess the accuracy of the PFT model. However, it was thought that the model presented in this contribution was sufficiently accurate for the description of microstructure formation in complex systems, especially considering the other unknowns and uncertainties.

3.3. Application to Al–Mg–Si

The model was then used to predict microstructure formation in an Al–1 wt%Mg–1 wt%Si alloy under various cooling rate and inoculation conditions. A calculation domain containing several grains was used in order to investigate the effect of their interaction on their morphology and growth kinetics. Two calculations, D and E, with different grain densities [92 grains/mm² (D) and 18
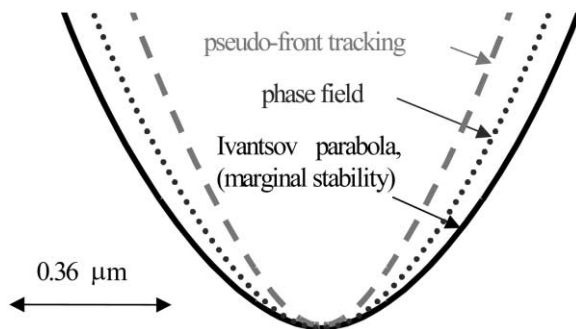
grains/mm^2 (E)] and different heat extraction rates ($\dot{H} = -39\text{MWm}^{-3}$(D) and $\dot{H} = -208\text{MWm}^{-3}$ (E), equivalent to cooling rates before solidification of –15 and –80Ks^{-1}, respectively) were performed. The calculations were started at the liquidus temperature and stopped when a monovariant line was reached. The thermodynamic data were obtained from the database of Ansara *et al.* [25]. Solid seeds were nucleated randomly in the 500 µm×433 µm calculation domain according to the selected grain density. The crystal orientation, θ_0, of each solid seed was chosen randomly and propagated to interfacial cells during growth. The other conditions of the calculations are listed in Table 1.

Fig. 9 illustrates the results of calculations D and E at different stages during solidification. Fig. 9(a)–(d) show the grain morphology and the concentration field of magnesium in the liquid, whereas Fig. 9(e) and (f) present the grain structure and the distribution of Mg in the solid phase. The latter figures correspond to the end of the calculation, when the phase Mg$_2$Si could precipitate.

In the case of low cooling rate and high grain density (calculation D, left of Fig. 9), it can be seen that the gradient of Mg concentration in the liquid drops very rapidly due to the overlap of the diffusion layers around the grains. As a result, the grains keep their globular morphology throughout the entire solidification process. In the case of high cooling rate and low grain density (calculation E, right of Fig. 9), interaction between the diffusion layers occurs later (except for liquid regions separating two close neighbour grains) and larger variations of Mg concentration are observed in the liquid. This situation leads to a destabilization of the solid–liquid interface and a dendritic grain morphology. A few dendrite tips can grow freely in the liquid without much influence from other growing tips. However, the diffusion fields start to overlap before fully developed dendrites can form. Some thermal noise was intentionally added in this calculation to enhance the formation of secondary arms. It was found however that the grain morphology is not much sensitive to noise. It was concluded that the overlap of the diffusion layers is responsible for the scarcity of secondary arms.

The solidification paths obtained for calculations D and E are presented on the ternary Al–Mg–Si phase diagram of Fig. 10. Although, the calculated paths do not differ much between the two cases, the influence of the density and morphology of the grains is clearly visible. Both calculations ended when the solidification path hit the Al–Mg$_2$Si-liquid monovariant line, i.e. when Mg$_2$Si particles could precipitate. However, in more complex systems, where the stability range of the secondary phases is smaller or for some critical alloy compositions, such a difference in the solidification conditions could lead to different secondary phases. Larger differences would also be expected between globular and fully dendritic microstructures.

The calculations presented above were repeated using the different strategies presented in Section 2.4 to couple the PFT model with THERMO-CALC. As anticipated, no significant differences were observed between the results obtained with the three strategies, except for the computation time! This indicates that the resolution used to tabulate the thermodynamic data is sufficient and that the assumption of local linear dependencies used to optimise the direct coupling is valid under the present conditions. The computation times reported in Table 3 indicate that a direct coupling is not more computationally intensive than a tabulation technique, provided a linearization procedure is used. The direct coupling without linearization leads to a substantial overhead in computation time. The later is however strongly influenced by the proportion of interfacial cells (higher in globular microstructure than in the dendritic one). Some robustness problems were experienced with the non-optimised direct coupling, due to sporadic numerical oscillations.

4. Conclusions

A new numerical model for the description of microstructure formation during solidification of multi-component systems has been developed. The model is based on an original technique to describe the evolution of interfaces that are governed by solute diffusion and Gibbs–Thomson effect. The model was coupled to a thermodynamic database using different strategies, in particular a computationally efficient direct coupling with the THERMO-CALC TQ interface.
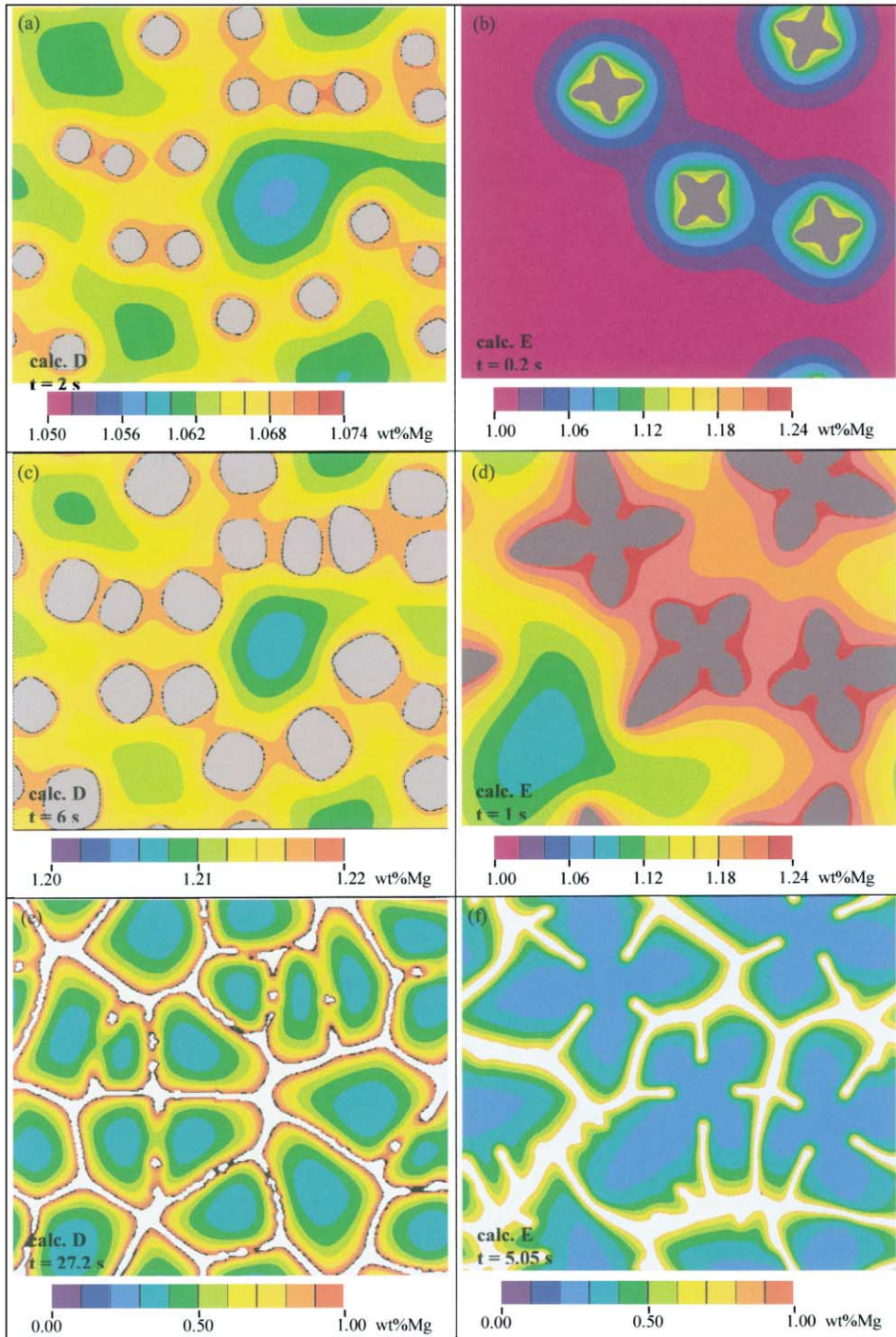
Fig. 9. Evolution of the microstructure and Mg concentration field during the formation of the primary phase in Al–1 wt%Mg–1wt%Si for two thermal and nucleation conditions (calculations D and E).
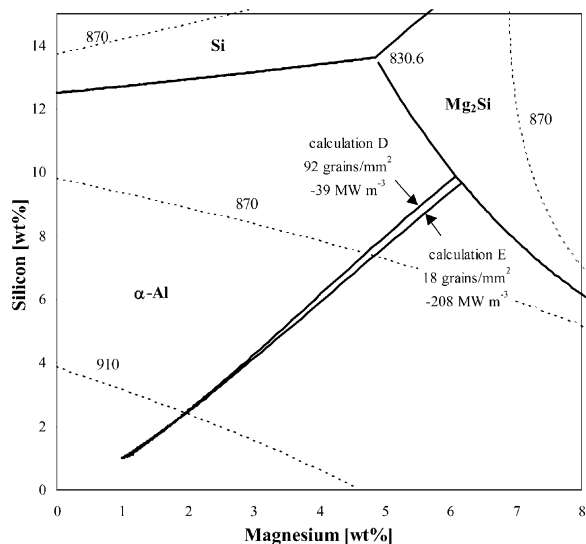
Fig. 10. Projection of the liquidus surface of the Al–Mg–Si alloy near the Al-rich corner and solidification paths obtained with the PFT model for two sets of nucleation and cooling conditions.

Table 3
CPU time of PFT calculations as a function of the method used to obtain phase diagram data (SGI R10000@250 MHz)

	Tabulated data (h)	Direct coupling with THERMO-CALC (h)	Optimised direct coupling with THERMO-CALC (h)
Globular	100	500[a]	70
Globulo-dendritic	107	200	112

[a] Extrapolated.

The results obtained with the model were validated against other approaches, such as marginal stability theory, a one-dimensional front-tracking method, and two-dimensional PF models for binary alloys. Good agreement was found for all the comparisons performed. Some discrepancy was observed between PF and PFT calculations for free dendritic growth at high undercooling. However, the differences could be explained qualitatively by considering the influence of attachment kinetics and solute trapping, which is neglected in PFT and certainly overestimated in the PF model. Further-more, excellent agreement is obtained between these two approaches at low undercooling, where the attachment kinetics contribution is much smaller.

PF simulations using realistic kinetic coefficients are generally difficult to perform. The absence of non-equilibrium effects in the PFT model is therefore a clear advantage to calculate microstructures in metallic systems under normal solidification conditions. On the other hand, the PFT method is more difficult to implement numerically due to the complex geometrical algorithm used to reconstruct the interface from the solid fraction field. It was also experienced that PFT simulations are about two to four times more computationally intensive than the PF ones for an equivalent number of nodes. However, the number of nodes needed to achieve a certain accuracy is not necessarily the same. A systematic investigation of the computational efficiency of each model was beyond the scope of this contribution. The first objective was to show the validity of this approach and, in this respect, the PFT method is believed to be an interesting alternative to other models of microstructure formation.

The PFT model was used successfully to describe various types of microstructures such as globular, globulo-dendritic and dendritic grains in a ternary aluminium alloy. In the case of aluminium alloys produced by direct chill semi-continuous casting, the microstructure has essentially a globular or globular-dendritic morphology with a very weak anisotropy of the interfacial energy. The present model provides an interesting tool for predicting the influence of alloy composition, casting conditions and inoculation on the resulting microstructure, microsegregation profiles, distribution of interdendritic phases. Although limited at present to primary phase solidification, it is being extended to include precipitation of various phases once a monovariant line is reached and homogenization.

Acknowledgements

Appendix

Let us consider a mushy cell composed of a solid sub-domain, Ω_α, and of a liquid sub-domain, Ω_l, separated by an interface, $\Gamma_{\alpha/l}$ (see Fig. A1). Assuming a constant specific mass, the solute balance for element i over the cell domain $\Omega = \Omega_\alpha \cup \Omega_l$ can be expressed by:

$$\int_{\Gamma_\alpha} (\mathbf{J}_i^\alpha \cdot \mathbf{n}) d\Gamma + \int_{\Gamma_l} (\mathbf{J}_i^l \cdot \mathbf{n}) d\Gamma = -\frac{d}{dt} \int_\Omega w_i d\Omega \qquad (A1)$$

where Γ_α and Γ_l are the external boundaries of Ω_α and Ω_l, $\mathbf{J}_i^\alpha$ and $\mathbf{J}_i^l$ are the solute fluxes along Γ_α and Γ_l, respectively, $\mathbf{n}$ is the unit vector normal to the boundaries, pointing outward of the domain. Introducing
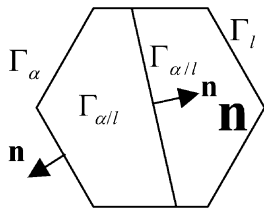

Fig. A1   Mushy cell.

$$\Phi_i^\alpha = -\int_{\Gamma_\alpha} (\mathbf{J}_i^\alpha \cdot \mathbf{n}) d\Gamma \text{ and } \Phi_i^l = \qquad (A2)$$

$$-\int_{\Gamma_l} (\mathbf{J}_i^l \cdot \mathbf{n}) d\Gamma$$

Eq. (A1) can be rewritten as:

$$\Phi_i^\alpha + \Phi_i^l = \frac{d}{dt} \int_{\Omega_\alpha(t)} w_i^\alpha d\Omega + \frac{d}{dt} \int_{\Omega_l(t)} w_i^l d\Omega \qquad (A3)$$

where $\Omega_\alpha(t)$ and $\Omega_l(t)$ express the time-dependence of the sub-domains. Developing (A3) yields:

$$\Phi_i^\alpha + \Phi_i^l = \int_{\Omega_\alpha(t)} \frac{\partial w_i^\alpha}{\partial t} d\Omega$$

$$+ \int_{\Gamma_{\alpha/l}} (w_i^\alpha \mathbf{v} \cdot \mathbf{n}) d\Gamma + \int_{\Omega_l(t)} \frac{\partial w_i^l}{\partial t} d\Omega \qquad (A4)$$

$$- \int_{\Gamma_{\alpha/l}} (w_i^l \mathbf{v} \cdot \mathbf{n}) d\Gamma$$

where $\mathbf{v}$ is the velocity of the interface and $\mathbf{n}$ along $\Gamma_{\alpha/l}$ is defined as pointing toward the liquid.

Assuming that the cell is small enough so that each quantity can be represented by a single value, we get:

$$\Phi_i^\alpha + \Phi_i^l = g_\alpha V \frac{\partial w_i^\alpha}{\partial t} + (1-g_\alpha) V \frac{\partial w_i^l}{\partial t} \qquad (A5)$$

$$+ \mathbf{v} \cdot \mathbf{n} \, (w_i^\alpha - w_i^l) S_{\alpha/l}$$

where $S_{\alpha/l}$ is the surface area of $\Gamma_{\alpha/l}$, V is the volume of the cell and g_α is the volume fraction of solid in the cell.

On the other hand, the PFT method is based on the following formulation:

$$\Phi_i^\alpha + \Phi_i^l = V \frac{dw_i}{dt} = V \frac{d}{dt} (g_\alpha w_i^\alpha + (1-g_\alpha) w_i^l) =$$

$$V \left[(w_i^\alpha - w_i^l) \frac{\partial g_\alpha}{\partial t} + g_\alpha \frac{\partial w_i^\alpha}{\partial t} + (1-g_\alpha) \frac{\partial w_i^l}{\partial t} \right]. \qquad (A6)$$

Considering also that

$$\mathbf{v} \cdot \mathbf{n} \, S_{\alpha/1} = V \frac{\partial g_\alpha}{\partial t} \tag{A7}$$

the equivalence between (A5) and (A6) is directly obtained. This justifies the formulation used in the model.

In order to establish the link between the PFT formulation and Eq. (2), we have to consider the two terms on the left hand side of Eq. (A5). When the size of the mushy cell tends toward zero, the continuity of fluxes in the α-phase imposes that:

$$\int_{\Gamma_\alpha} (\mathbf{J}_i^\alpha \cdot \mathbf{n}) \mathrm{d}\Gamma + \int_{\Gamma_{\alpha/1}} (\mathbf{J}_i^\alpha \cdot \mathbf{n}) \mathrm{d}\Gamma = 0. \tag{A8}$$

Therefore

$$\Phi_i^\alpha = (\mathbf{J}_i^\alpha \cdot \mathbf{n}) \, S_{\alpha/1}. \tag{A9}$$

Similarly, in the liquid phase:

$$\int_{\Gamma_1} (\mathbf{J}_i^1 \cdot \mathbf{n}) \mathrm{d}\Gamma - \int_{\Gamma_{\alpha/1}} (\mathbf{J}_i^1 \cdot \mathbf{n}) \mathrm{d}\Gamma = 0 \tag{A10}$$

and

$$\Phi_i^1 = -\mathbf{J}_i^1 \cdot \mathbf{n} \, S_{\alpha/1}. \tag{A11}$$

Inserting (A9) and (A11) into (A5) yields:

$$(\mathbf{J}_i^\alpha - \mathbf{J}_i^1) \cdot \mathbf{n} \, S_{\alpha/1} = V \left(g_\alpha \frac{\partial w_i^\alpha}{\partial t} + (1 - g_\alpha) \frac{\partial w_i^1}{\partial t} \right)$$

$$+ (w_i^\alpha - w_i^1) \mathbf{v} \cdot \mathbf{n} \, S_{\alpha/1}. \tag{A12}$$

For a vanishing cell size, $V/S_{\alpha/1} \rightarrow 0$ and (A12) becomes:

$$(\mathbf{J}_i^\alpha - \mathbf{J}_i^1) \cdot \mathbf{n} = (w_i^1 - w_i^\alpha) \mathbf{v} \cdot \mathbf{n} \tag{A13}$$

which is equivalent to Eq. (2) if Fick's first law is used to formulate the fluxes.

References

[1] Sundman B, Jansson B, Andersson JO. CALPHAD 1985;9:153.

[2] Saito Y, Goldbeck-Wood G, Muller-Krumbhaar H. Phys Rev A 1988;38:2148.

[3] Lynch DR. J Comp Phys 1982;47:387.

[4] Jacot A, Rappaz M, Reed RC. Acta Mater 1998;46:3949.

[5] Kobayashi R. Phys D 1993;63:410.

[6] Karma A, Rappel WJ. J Crystal Growth 1997;174:54.

[7] Warren JA, Boettinger WJ. Acta Metall 1995;43:689.

[8] Tiaden J, Nestler B, Diepers HJ, Steinbach I. Phys D 1998;115:73.

[9] Provatas N, Goldenfeld N, Dantzig J. J Phys Rev Lett 1998;80:3308.

[10] Karma A. Phys Rev. E 1194;49:2245.

[11] Henry S. PhD thesis, No. 1943, Ecole Polytechnique Fédérale de Lausanne, Switzerland; 1999.

[12] Grafe U, Boettger B, Tiaden J, Fries SG, Steinbach I. In: Sahm PR, Hansen PN, Conley JG, editors. Modeling of Casting, Welding and Advanced Solidification Processes IX, Aachen (D); 2000. p. 481–488.

[13] Nestler B, Wheeler AA. Phys D 2000;138:114–33.

[14] Dantzig JA, Provatas N, Goldenfeld N, LaCombe JC, Lupulescu A, Koss MB, Glicksmann ME. In: Modeling of Casting, Welding and Advanced Solidification Processes IX, Aachen (D); 2000. p. 453–460.

[15] Karma A. Phys Rev E 1998;57:4323.

[16] Karma A, Rappel WJ. Phys Rev E 1996;53:R3017.

[17] Jacot A, Rappaz M. Acta Mater 1997;45:575.

[18] Dilthey U, Pavlik V. In: Thomas BG, Beckermann C, editor. Modeling of Casting and Advanced Solidification Processes VIII. TMS; 1998. p. 589.

[19] Juric D, Tryggvason G. J Comp Phys 1996;123:127.

[20] Kothe DB, Rider WJ, Mosso SJ, Brock JS. Internal report, Los Alamos Research Laboratories; 1996.

[21] Doré X. Modélisation de la microségrégation et de l'homogénéisation dans les alliages multicomposés: application au système Al–Mg–Si. Ph. D. Thesis No 2143, Ecole Polytechnique Fédérale de Lausanne; 2000

[22] CALPHAD, Computer coupling of phase diagrams and thermochemistry; 1999.

[23] Kurz W, Fisher DJ. Fundamentals of solidification. Zürich: Trans Tech Publications, 1989.

[24] Ben Amar M. Phys Rev A 1990;41:2080.

[25] Ansara I, Dinsdale AT, Rand MH. EUR000018171-COST 507. Definition of thermochemical and thermophysical properties to provide a database for the development of new light alloys. Proceedings of the final workshop, Vaals, the Netherlands, 9 to 12 March 1997, EUR-OP Office for Publications, Luxembourg, 1998. ISBN 92-828-3901-X.

[26] Bakker H. Diffusion in solid metals alloys. Berlin: Springer/Landolt-Börnstein, 1990.

[27] Kovakowa K, German D. Giessereiforschung 1979;23:169.

[28] Körber K, Löhberg K. Mater 1979;17:144.

Erratum

A pseudo-front tracking technique for the modelling of solidification microstructures in multi-component alloys [Acta Materialia 50(8), pp. 1909 - 1926]☆

A Jacot [a,b], M Rappaz [a]

[a] *Laboratoire de Métallurgie Physique, MX-G, Ecole Polytechnique Fédérale de Lausanne, 1015 Lausanne, Switzerland*
[b] *Calcom SA, Parc Scientifique, Ecole Polytechnique Fédérale de Lausanne, CH-1015 Lausanne, Switzerland*

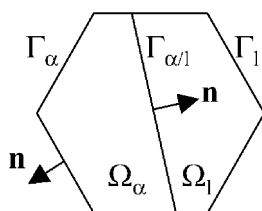Fig. A1 of the above paper was unfortunately published incorrectly. Please find the correct version below.

Fig. A1. Mushy cell.